OPEN ACCESS



Improving the Alfvén Wave Solar Atmosphere Model Based on Parker Solar Probe Data

B. van der Holst 1, J. Huang 1, N. Sachdeva 1, J. C. Kasper 1, W. B. Manchester IV 1, D. Borovikov 2, V. B. D. G. Chandran², A. W. Case³, K. E. Korreck³, D. Larson⁴, R. Livi⁴, M. Stevens³, P. Whittlesey⁴, S. D. Bale^{5,6,7,8}, M. Pulupa⁶, D. M. Malaspina^{9,10}, J. W. Bonnell⁶, P. R. Harvey⁶, K. Goetz¹¹, and R. J. MacDowall¹² Climate and Space Sciences and Engineering, University of Michigan, Ann Arbor, MI 48109, USA ² Space Science Center and Department of Physics, University of New Hampshire, Durham, NH 03824, USA Smithsonian Astrophysical Observatory, Cambridge, MA 02138 USA University of California, Berkeley: Berkeley, CA 94720, USA ⁵ Physics Department, University of California, Berkeley, CA 94720-7300, USA ⁶ Space Sciences Laboratory, University of California, Berkeley, CA 94720-7450, USA The Blackett Laboratory, Imperial College London, London, SW7 2AZ, UK ⁸ School of Physics and Astronomy, Queen Mary University of London, London E1 4NS, UK Astrophysical and Planetary Sciences Department, University of Colorado, Boulder, CO 80309, USA Laboratory for Atmospheric and Space Physics, University of Colorado, Boulder, CO 80303, USA ¹¹ School of Physics and Astronomy, University of Minnesota, Minneapolis, MN 55455, USA ¹² Solar System Exploration Division, NASA/Goddard Space Flight Center, Greenbelt, MD 20771, USA Received 2021 May 20; revised 2021 November 22; accepted 2021 November 23; published 2022 February 2

Abstract

In van der Holst et al. (2019), we modeled the solar corona and inner heliosphere of the first encounter of NASA's Parker Solar Probe (PSP) using the Alfvén Wave Solar atmosphere Model (AWSoM) with Air Force Data Assimilative Photospheric flux Transport–Global Oscillation Network Group magnetograms, and made predictions of the state of the solar wind plasma for the first encounter. AWSoM uses low-frequency Alfvén wave turbulence to address the coronal heating and acceleration. Here, we revise our simulations, by introducing improvements in the energy partitioning of the wave dissipation to the electron and anisotropic proton heating and using a better grid design. We compare the new AWSoM results with the PSP data and find improved agreement with the magnetic field, turbulence level, and parallel proton plasma beta. To deduce the sources of the solar wind observed by PSP, we use the AWSoM model to determine the field line connectivity between PSP locations near the perihelion at 2018 November 6 UT 03:27 and the solar surface. Close to the perihelion, the field lines trace back to a negative-polarity region about the equator.

Unified Astronomy Thesaurus concepts: Solar wind (1534); Magnetohydrodynamics (1964)

1. Introduction

The Parker Solar Probe (PSP; Fox et al. 2016) was successfully launched on 2018 August 12 with the goal of better understanding the space environment in the outer corona. PSP has already sent back a wealth of unprecedented high-cadence data from closer to the Sun than any spacecraft before. PSP caries four instruments. Two of them, the Solar Wind Electrons Alphas and Protons (SWEAP; Kasper et al. 2016) and Fields Experiment (FIELDS; Bale et al. 2016), observe in situ the thermal plasma distribution, magnetic field, and Alfvén wave turbulence. These data provide an opportunity to compare solar wind models with in situ observations of the outer corona plasma and improve the models accordingly.

PSP has inspired a a number of studies, which predict, interpret, and provide context for its close-in observations. Riley et al. (2019) used the Magnetohydrodynamic Around a Sphere (MAS) model to make predictions of the plasma state along the spacecraft trajectory, and additionally mapped field lines from the PSP locations back to the solar surface to infer the source of the solar wind. Improved simulations for the first four PSP encounters were shown in Riley et al. (2021), where their thermodynamic model provided the best match relative to their polytropic and wave turbulence model. Xiong et al. (2018)

Original content from this work may be used under the terms of the Creative Commons Attribution 4.0 licence. Any further distribution of this work must maintain attribution to the author(s) and the title of the work, journal citation and DOI.

performed forward modeling using conservation element and solution element multidimensional magnetohydrodynamics (MHD) to make PSP predictions based on the solar minimum Carrington rotation 2060. Chhiber et al. (2019a) used a 3D MHD model with turbulence to provide context for their prediction of how much time PSP would spend inside the sonic, Alfvén, and plasma beta equal one surfaces. These simulations were performed for nontilted and tilted dipole as well as magnetogram-based inner boundary conditions to determine the degree of sensitivity of the boundary input. In Chhiber et al. (2019b), a context prediction was provided for turbulence properties and the accuracy of the Taylor hypothesis along the PSP trajectory. Badman et al. (2020) examined PSP magnetic field connectivity to the solar surface in terms of source surface heights. Al-Haddad et al. (2019) analyzed 3D simulated coronal mass ejections (CMEs) in the innermost heliosphere, below 0.29 au, to predict CME properties for PSP. Vásquez et al. (2019) analyzed the feasibility of tomographic reconstruction of the coronal electron density using time series of white-light total brightness images of the Wide-field Imager for Solar Probe instrument (WISPR; Vourlidas et al. 2016) for each of the selected orbits. They used the Alfvén Wave Solar atmosphere Model (AWSoM; van der Holst et al. 2014) to construct synthetic images mimicking the WISPR observations to perform such a study. Liewer et al. (2019) used series of synthetic whitelight images to analyze if it is possible to determine 3D coronal density information using WISPR.

van der Holst et al. (2019) used the AWSoM to predict the time-independent solar corona and inner heliosphere during the first PSP encounter as well as the plasma state along the spacecraft trajectory, which was performed prior to the public release of any PSP data. Now, with the PSP data made available, we are able to validate the model output. We find that our predictions were highly accurate in predicting the solar wind speed, current sheet crossings, and, perhaps most significantly, the Alfvénic turbulence levels. However, we also find discrepancies in the forms of too-high plasma beta, a toolow proton temperature anisotropy, and a too-weak magnetic field strength. This motivated us to improve the model. The current paper addresses the field strength by increasing the resolution near the current sheet, and partially addresses the temperature anisotropy and plasma beta by improving the energy partitioning.

The AWSoM model (van der Holst et al. 2014) is a 3D MHD model for the solar corona and inner heliosphere, with coronal heating and solar wind acceleration provided by low-frequency, reflection-driven Alfvén wave turbulence. The model is datadriven by inserting a magnetogram at the inner boundary. Over the years, we have performed extensive validation studies of AWSoM, and mention here two recent examples. Szente et al. (2019) developed the SPECTRUM postprocessing tool that calculates synthetic spectra for the AWSoM model, and compared the spectra with the observations made with the Hinode/Extreme-ultraviolet Imaging Spectrometer. Sachdeva et al. (2019) validated AWSoM against various in situ and remote-sensing observational data sources. In the low corona, they compared AWSoM model results with the EUV images and 3D tomographic reconstructions of the electron temperature and density from Solar TErrestrial RElations Observatory (STEREO)-A/Extreme UltraViolet Imager, Solar Dynamics Observatory (SDO)/Atmospheric Imaging Assembly (AIA), and Solar and Heliospheric Observatory (SOHO)/Large Angle and Spectromeric Coronagraph Experiment (LASCO) observations. Farther out in the heliosphere, the AWSoM predicted solar wind speed was found to agree well with the velocity reconstructions from InterPlanetary Scintillation (IPS) observations and OMNI data near the Earth. These studies found AWSoM capable of reproducing the observed plasma density, temperature, and velocity at distances ranging from 1.01 R_s to 1 au.

Our paper is organized as follows. We first provide a summary of the physics used in the AWSoM model. In Section 3, we present details of the improvements in the energy partitioning as implemented. In Section 4, we compare the model output with the PSP data from the FIELDS and SWEAP instruments. This validation is along the PSP trajectory for the first encounter with perihelion at 2018 November 6 UT 3:27. Here, we also map the locations of PSP back to the solar surface via field line tracing to determine the origin of the solar wind. We summarize our findings in Section 5.

2. AWSoM Model

In the AWSoM model, we solve for the full set of MHD equations with proton temperature anisotropy, augmented with equations for the low-frequency Alfvén wave turbulence. Here, we summarize these equations. For a full derivation of the used wave turbulence, the reader is referred to van der Holst et al. (2014). In the inertial frame, the conservation of mass,

conservation of momentum, and induction equation are

$$\frac{\partial \rho}{\partial t} + \nabla \cdot (\rho \mathbf{u}) = 0, \tag{1}$$

$$\frac{\partial \rho \mathbf{u}}{\partial t} + \nabla \cdot \left[\rho \mathbf{u} \mathbf{u} + (P_{\parallel p} - P_{\perp p}) \mathbf{b} \mathbf{b} - \frac{1}{\mu_0} \mathbf{B} \mathbf{B} \right]$$

$$+ \nabla \left(P_{\perp p} + P_e + \frac{B^2}{2\mu_0} + P_A \right) = -\rho \frac{GM_{\odot}}{R^3} \mathbf{R}, \tag{2}$$

$$\frac{\partial \mathbf{B}}{\partial t} - \nabla \times (\mathbf{u} \times \mathbf{B}) = 0, \tag{3}$$

where ρ is the mass density, \boldsymbol{u} is the bulk speed for both the protons and electrons, \boldsymbol{B} is the magnetic field, G is the gravitational constant, M_{\odot} is the mass of the Sun, \boldsymbol{R} is the position vector relative to the center of the Sun, P_A is the Alfvén wave pressure, and μ_0 is the permeability of vacuum. The electron pressure P_e is assumed to be isotropic. The proton pressure tensor \boldsymbol{P}_p is decomposed into a pressure component parallel to the magnetic field $P_{\parallel p}$ and a pressure component perpendicular to the magnetic field $P_{\perp p}$, so that $\boldsymbol{P}_p = P_{\perp p}\boldsymbol{I} + (P_{\parallel p} - P_{\perp p})\boldsymbol{b}\boldsymbol{b}$, where $\boldsymbol{b} = \boldsymbol{B}/B$. Instead of solving for the perpendicular proton pressure, we solve for the averaged proton pressure $P_p = (2P_{\perp p} + P_{\parallel p})/3$ and recast the equation into a full energy equation

$$\frac{\partial}{\partial t} \left(\frac{P_p}{\gamma - 1} + \frac{\rho u^2}{2} + \frac{B^2}{2\mu_0} \right)
+ \nabla \cdot \left[\left(\frac{\rho u^2}{2} + \frac{P_p}{\gamma - 1} + \frac{B^2}{\mu_0} \right) \boldsymbol{u} + \boldsymbol{P}_p \cdot \boldsymbol{u} \right]
- \frac{\boldsymbol{B}(\boldsymbol{u} \cdot \boldsymbol{B})}{\mu_0}$$

$$= -\boldsymbol{u} \cdot \nabla (P_e + P_A) + \frac{N_p k_B}{\tau_{ep}} (T_e - T_p)
+ Q_p - \rho \frac{GM_{\odot}}{R^3} \boldsymbol{R} \cdot \boldsymbol{u}, \tag{4}$$

where $N_{e,p} = \rho/m_p$ are the electron and proton number densities and m_p is the proton mass, and $T_{e,p}$ are the electron and proton temperatures that are obtained from the equation-of-state $P_{e,p} = N_{e,p}k_BT_{e,p}$. The adiabatic index is assumed to be $\gamma = 5/3$. The second term on the right-hand side is the Coulomb collisional energy exchange between the protons and electrons, which is inversely proportional to the relaxation time τ_{ep} . The third term is the proton heating function Q_p . The time evolution for the parallel proton temperature is obtained from

$$\frac{\partial P_{\parallel p}}{\partial t} + \nabla \cdot (P_{\parallel p} \boldsymbol{u}) + 2P_{\parallel p} \boldsymbol{b} \cdot (\nabla \boldsymbol{u}) \cdot \boldsymbol{b}$$

$$= \frac{\delta P_{\parallel p}}{\delta t} + 2\frac{N_p k_B}{\tau_{ep}} (T_e - T_{\parallel p}) + 2Q_{\parallel p}, \tag{5}$$

where the first term on the right-hand side is the relaxation source term for the pressure anisotropy. If the plasma exceeds the stability threshold of the mirror (Tajiri 1967), protoncyclotron (Kennel & Petschek 1966), and Chew, Goldberger, and Low (CGL) firehose (Chew et al. 1956), the plasma is

relaxed back to the marginal stable state using a relaxation time that is inversely proportional to the growth rate of these instabilities. The second term is the collisional energy exchange with the electrons, while the third term is the heating function $Q_{\parallel p}$ for the parallel proton temperature. The energy equation for the electrons reads

$$\frac{\partial}{\partial t} \left(\frac{P_e}{\gamma - 1} \right) + \nabla \cdot \left(\frac{P_e}{\gamma - 1} \boldsymbol{u} \right) + P_e \nabla \cdot \boldsymbol{u}$$

$$= -\nabla \cdot \boldsymbol{q}_e + \frac{N_p k_B}{\tau_{ep}} (T_p - T_e) - Q_{\text{rad}} + Q_e. \tag{6}$$

Here, $Q_{\rm rad} = N_e N_p \Lambda(T_e)$ is the optically thin radiative energy loss, and Q_e is the heating function for the electron temperature. The electron heat conduction q_e transitions around $R = 5R_{\odot}$ from the collision heat conduction formulation of Spitzer & Härm (1953) along the field lines to the collisionless heat flux formulated by Hollweg (1978), as described in van der Holst et al. (2014).

The Alfvén wave pressure P_A and the coronal heating functions Q_e , Q_p , and $Q_{\parallel p}$ are obtained from the wave turbulence equations describing the advection, compression, reflection, and dissipation of the wave energy densities w_{\pm} , where the + sign is for Alfvén waves propagating in the direction of the magnetic field and - is for waves propagating in the opposite direction. These equations were derived in van der Holst et al. (2014) with an approach analogous to Matthaeus et al. (1999), Velli (1993), Zank et al. (1996), Chandran & Hollweg (2009), and Chandran et al. (2009):

$$\frac{\partial w_{\pm}}{\partial t} + \nabla \cdot [(\boldsymbol{u} \pm \boldsymbol{V}_{A})w_{\pm}] + \frac{w_{\pm}}{2}(\nabla \cdot \boldsymbol{u})
= \mp \mathcal{R} \sqrt{w_{-}w_{+}} - \Gamma_{\pm}w_{\pm}.$$
(7)

The first two terms on the left-hand side represent the propagation along the field lines, in which we have used the Alfvén speed $V_A = B/\sqrt{\mu_0\rho}$. The third term is the wave energy reduction in the expanding flow due to work done by the wave pressure $P_A = (w_+ + w_-)/2$. The second term on the right-hand side is the wave dissipation rate, which is in our model similar to the phenomenological cascade rate model of Dmitruk et al. (2002),

$$\Gamma_{\pm} = \frac{2}{L_{\parallel}} \sqrt{\frac{w_{\mp}}{\rho}}, \tag{8}$$

in which we assume the dependence of the perpendicular correlation length $L_{\perp} \propto \sqrt{B}$ similar to Hollweg (1986). The first term on the right-hand side is the reflection term describing the conversion into the oppositely propagating wave energy densities. The signed reflection coefficient was derived in van der Holst et al. (2014) in an approach similar to Matthaeus et al. (1999):

$$\mathcal{R} = \min \left[\mathcal{R}_{\text{imb}}, \max(\Gamma_{\pm}) \right] \left[\max \left(1 - 2\sqrt{\frac{w_{-}}{w_{+}}}, 0 \right) - \max \left(1 - 2\sqrt{\frac{w_{+}}{w_{-}}}, 0 \right) \right]. \tag{9}$$

Here.

$$\mathcal{R}_{imb} = \sqrt{[\boldsymbol{b} \cdot (\nabla \times \boldsymbol{u})]^2 + [(\boldsymbol{V}_A \cdot \nabla) \log \boldsymbol{V}_A]^2}, \quad (10)$$

is the part of the reflection rate that applies to the imbalanced turbulence. This shows that the wave reflection in our model is due to the Alfvén speed gradient and field-aligned vorticity. We additionally assume as in van der Holst et al. (2014) that the reflection rate is smaller than the maximum dissipation rate. The second square bracket is a correction when the oppositely propagating waves are of equal wave energy density, in which case we assume the reflection rate to be negligible.

3. Improved Energy Partitioning

We describe here the improvements in the energy partitioning of the AWSoM model. The main changes in the model are summarized as follows: (1) the alignment angle between the counterpropagating Alfvén waves is now included in the energy cascade; and (2) we now use the critical-balance formulation of Lithwick et al. (2007). We give details of the changes below, but for clarity and future references we give a more complete description of the energy partitioning.

The expression of the Alfvén wave energy density at length scale λ was shown in Chandran et al. (2011). For completeness, we provide here a derivation. In Boldyrev (2005), it was shown that for $z_{\pm,\lambda}$ at length scale λ the cascade time at that length scale is

$$\tau_{\pm,\lambda} = \frac{\lambda}{z_{\pm,\lambda}\sin(\theta_{\lambda})},\tag{11}$$

which is dependent on the alignment angle θ_{λ} at length scale λ and the Alfvén wave amplitude of the oppositely propagating wave at that length scale. We further assume that the energy-cascade rate Q_{\pm} is in the inertial range independent of the length scale

$$Q_{\pm,\lambda} = \frac{w_{\pm,\lambda}}{\tau_{\pm,\lambda}} \propto \lambda^0,\tag{12}$$

hence $Q_{\pm,\lambda} = Q_{\pm,L_{\perp}}$. Combining Equations (11) and (12) results in

$$\frac{Q_{\pm,\lambda}}{Q_{\pm,L_{\perp}}} = 1 = \frac{w_{\pm,\lambda}}{w_{\pm,L_{\perp}}} \sqrt{\frac{w_{\mp,\lambda}}{w_{\mp,L_{\perp}}}} \frac{L_{\perp} \sin(\theta_{\lambda})}{\lambda \sin(\theta_{L_{\perp}})}.$$
 (13)

Under the assumption of small angle approximation (which is not necessarily true at the outer scale L_{\perp}) and using the angle scaling derived by Boldyrev (2005), i.e., $\theta_{\lambda} \propto \lambda^{1/4}$, we arrive at

$$\frac{w_{\pm,\lambda}}{w_{\pm,L_{\perp}}} \sqrt{\frac{w_{\mp,\lambda}}{w_{\mp,L_{\perp}}}} \left(\frac{L_{\perp}}{\lambda}\right)^{3/4} = 1.$$
 (14)

From which we derive that

$$w_{\pm,\lambda} = w_{\pm,L_{\perp}} \sqrt{\frac{\lambda}{L_{\perp}}}, \tag{15}$$

in the inertial range.

The partial reflection of Alfvén waves results in counter-propagating waves. The nonlinear interaction of these oppositely directed waves causes a transverse energy cascade from the large outer scale L_{\perp} through the self-similar inertial range to smaller perpendicular scales, i.e., larger perpendicular wavenumber k_{\perp} , where dissipation takes place. When Alfvén waves

cascade to the gyroradius scale, the cascade transitions into a kinetic Alfvén wave (KAW) cascade. Some of the cascaded energy dissipates at $k_{\perp}r_{p} \sim 1$, where $r_{p} = V_{\perp p}/\Omega_{p}$ is the proton gyroradius, and $V_{\perp p} = \sqrt{2k_BT_{\perp p}/m_p}$ and $\Omega_p = (e/m_p)B$ are the proton perpendicular thermal speed and proton-cyclotron frequency, respectively, while m_p is the proton mass, e is the elementary charge, k_B is the Boltzmann constant, and $T_{\perp p}$ is the perpendicular proton temperature. Some of the energy cascades to and dissipates at even smaller scales. We will make the approximation that the dissipation of KAWs takes place in two distinct wavelength ranges: $k_{\perp}r_p \sim 1$ and $k_{\perp}r_p \gg 1$, which was also assumed for PSP observations in Bowen et al. (2020) and Chen et al. (2020). For the apportioning of this dissipation into the coronal heating functions Q_e , $Q_{\parallel p}$, and $Q_{\perp p}$ for the electron, parallel proton, and perpendicular proton heating, we employ the linear wave damping and nonlinear stochastic heating developed in Chandran et al. (2011). For collisionless plasma turbulence with large amplitude fluctuations, $\delta B \sim B$, where δB is the amplitude of the magnetic fluctuations and B the background magnetic field, damping rates from linear theory are generally smaller, or comparable to, the nonlinear frequencies of turbulence (Gary et al. 2020). In that scenario, the energy partitioning in the AWSoM model may no longer hold, but we will still use this energy partitioning since it has several freely adjustable parameters. We will check the $\delta B/B$ parameter in Section 4.

At $k_{\perp}r_{p} \sim 1$, we assume nonlinear damping of KAWs through stochastic heating of protons, which will result in perpendicular proton heating, as well as linear Landau damping and linear transit time damping of KAWs (Chandran et al. 2011). For the stochastic heating, we first need to determine the velocity perturbation $\delta u_{r_{p}}$ and the magnetic field perturbation $\delta B_{r_{p}}$ at the proton gyroradius scale. By assuming equipartition at the proton gyroscale, we obtain from Equation (15)

$$\rho \delta u_{r_p}^2 = w_{r_p}, \qquad \delta B_{r_p}^2 / \mu_0 = w_{r_p},$$
 (16)

where

$$w_{r_p} = w_{+,r_p} + w_{-,r_p} = (w_+ + w_-) \sqrt{\frac{r_p}{L_1}},$$
 (17)

is the total wave energy density at the proton gyroscale. The effective damping rate at $k_\perp r_p \sim 1$ from stochastic proton heating is

$$\gamma_{\perp p} = \frac{Q_{\text{stoch}}}{w_{r_p}} = c_1 \frac{\rho \delta u_{r_p}^3}{r_p w_{r_p}} \exp\left(-\frac{c_2}{\varepsilon_p}\right) + \sigma_1 \frac{\rho \delta u_{r_p}^3}{r_p w_{r_p}} \sqrt{\beta_p} \exp\left(-\frac{\sigma_2}{\delta_p}\right), \tag{18}$$

where c_1 , c_2 , σ_1 , and σ_2 are dimensionless constants of order unity, $\varepsilon_p = \delta u_{r_p}/V_{\perp p}$, and the stochasticity parameter $\delta_p = \delta B_{r_p}/B$. The first term on the right-hand side is the stochastic heating for $\beta_p = 2\mu_0 p_p/B^2 \lesssim 1$ (Chandran et al. 2011), while the second term is the stochastic heating for $1 < \beta_p < 30$ (Hoppock et al. 2018).

The linear Landau damping and linear transit time damping of KAWs contribute to the electron and parallel proton heating, respectively. Their damping rates at $k_{\perp}r_{p}\sim1$ onto the component

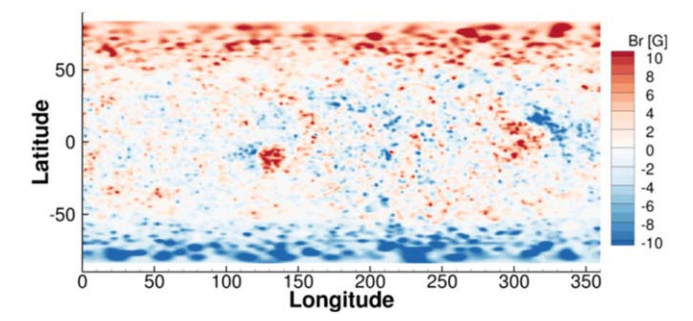


Figure 1. First realization of the ADAPT–GONG map in Carrington coordinates for the photospheric radial magnetic field component at time 2018 November 6 UT 04:00. For the purpose of showing both the active regions and coronal holes, we have saturated the magnetic field in this plot at $\pm 10~\rm G$.

Table 1
The Model Parameters

	Value	
$\overline{N_{\odot}}$	$2 \times 10^{17} \mathrm{m}^{-3}$	
N_{\odot} T_{\odot}	50, 000 K	
$(S_A/B)_{\odot}$	$10^6 \mathrm{W} \mathrm{m}^{-2} \mathrm{T}^{-1}$	
$L_{\!\perp}\sqrt{B}$	$1.5 \times 10^5 \mathrm{m} \sqrt{\mathrm{T}}$	
c_1	0.18	
c_2	0.21	
σ_1	1.17	
σ_2	0.21	

species are taken from Chandran et al. (2011)

$$\frac{\gamma_{\parallel e}}{|k_{\parallel} V_A|} = 0.01 \left(\frac{p_e}{p_p \beta_p} \right)^{1/2} \left[\frac{1 + 0.17 \beta_p^{1.3}}{1 + (2800 \beta_e)^{-1.25}} \right], \tag{19}$$

$$\frac{\gamma_{\parallel p}}{|k_{\parallel} V_A|} = 0.08 \left(\frac{p_e}{p_p}\right)^{1/4} \beta_p^{0.7} \exp\left(-\frac{1.3}{\beta_p}\right),\tag{20}$$

where $\beta_e = 2\mu_0 p_e/B^2$ is the electron plasma beta and p_e and p_p are the electron and proton pressure, respectively. At $k_\perp r_p \sim 1$, the KAW turbulence has a range of k_\parallel values, but for the damping rates $\gamma_{\parallel e}$ and $\gamma_{\parallel p}$ we assign similar to Chandran et al. (2011) a single k_\parallel determined by the critical-balance condition (Lithwick et al. 2007; Goldreich & Sridhar 1995)

$$k_{\parallel}V_A = 1/\tau_{\text{minor},r_p},\tag{21}$$

i.e., the wave period is set equal to the cascade time of the minor wave. Here, major and minor waves are determined by $w_{\text{major}} = \max(w_+, w_-)$ and $w_{\text{minor}} = \min(w_+, w_-)$. The cascade timescale for the minor wave at $k_{\perp}r_p = 1$ is then

$$\tau_{\text{minor},r_p} = \frac{r_p}{z_{\text{major},r_p} \sin(\theta_{r_p})} = \frac{w_{\text{minor},r_p}}{Q_{\text{minor}}},$$
 (22)

where we have used $Q_{\min r,r_p} = Q_{\min r}$. We note that we used $\tau_{\min r,r_p}$ in van der Holst et al. (2014), while we use $\tau_{\min r,r_p}$ in the present paper. This change increases the heating due to linear Landau damping and transit time damping of KAWs, hence there is more electron and parallel proton heating. We can also define the fraction of cascade power dissipated at

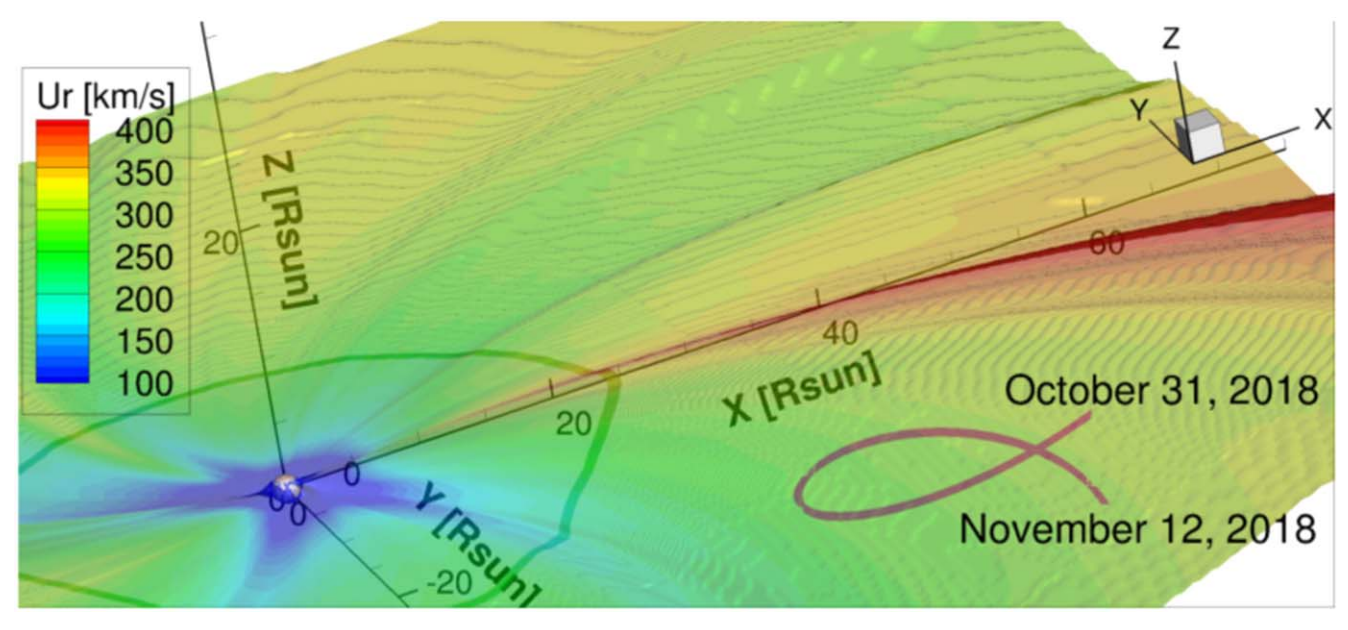


Figure 2. Heliospheric current sheet colored with radial solar wind speed. The magenta line is the PSP trajectory in the frame corotating with the Sun. The (X, Y, Z) coordinates in the HGR system are normalized to the solar radius.

 $k_{\perp}r_{p}\sim 1$ as

$$\Gamma_{\pm,r_p} = \frac{\gamma_{r_p} \tau_{\pm,r_p}}{1 + \gamma_{r_n} \tau_{\pm,r_p}},\tag{23}$$

where

$$\gamma_{r_p} = \gamma_{\perp p} + \gamma_{\parallel p} + \gamma_{\parallel e} \tag{24}$$

is the total effective damping rate of KAWs at $k_{\perp}r_p = 1$.

The final heating functions are expressed in terms of the heating fractions and damping rates via

$$Q_{\perp p} = \frac{\gamma_{\perp p}}{\gamma_{r_p}} Q_{r_p}, \qquad Q_{\parallel p} = \frac{\gamma_{\parallel p}}{\gamma_{r_p}} Q_{r_p}, \tag{25}$$

$$Q_e = \frac{\gamma_{\parallel e}}{\gamma_{r_p}} Q_{r_p} + (Q - Q_{r_p}), \tag{26}$$

where we defined

$$Q_{r_p} = \Gamma_{+,r_p} Q_+ + \Gamma_{-,r_p} Q_-, \ Q = Q_+ + Q_-.$$
 (27)

The last term in Equation (26) is for the remaining cascading power that cascades to $k_{\perp}r_{p}\gg1$, for which we assume that the dissipation is via interactions with the electrons, so that it contributes to electron heating.

4. Results

To obtain the steady-state background solution, we need to specify the radial magnetic field component at the inner boundary located in the lower transition region at 50,000 K. For that purpose, we use the synchronic magnetic maps obtained by the Air Force Data Assimilative Photospheric flux Transport (ADAPT) model (Henney et al. 2012; Hickmann et al. 2015) applied to Global Oscillation Network Group (GONG) maps. ADAPT employs a flux transport model to predict radial magnetic fields for the regions where data are not available. Different specifications of the supergranulation transport result in 12 realizations. Here, we use the first realization, which was also used in our previous prediction results (van der Holst et al. 2019).

This map, shown in Figure 1, has central meridian time 2018 November 6 UT 4:00.

The isotropic electron and parallel and perpendicular proton temperatures are all set to 50, 000 K uniformly at the inner boundary. The proton number density is set to $N_p = 2 \times 10^{17} \, \mathrm{m}^{-3}$ at the inner boundary. We overestimate the density at 50,000 K to provide a reservoir plasma that will not be depleted by chromospheric evaporation. We let this density first exponentially fall off to the correct level by means of flooring the temperature by 50,000 K from below, in a similar fashion to Lionello et al. (2009). The temperature and densities reach values consistent with those reconstructed from SDO/AIA-derived differential emission measure near a height of 1.02 R_{\odot} , as shown in Sachdeva et al. (2019).

The energy density of the outbound Alfvén waves at the inner boundary is set via the Poynting flux S_A of the outgoing waves: $w = (S_A/B)_{\odot} \sqrt{\mu_0 \rho}$, where B_{\odot} is the magnetic field strength at the inner boundary. We set the Poynting flux to field strength ratio to $(S_A/B)_{\odot} = 10^6$ W m⁻² T⁻¹, which is compatible with the Hinode observations (De Pontieu et al. 2007), as shown by Sokolov et al. (2013). The inbound Alfvén waves are absorbed by setting the inward-propagating wave energy density to zero. For the simulation results in the present paper, we have used parameter values for the boundary values, turbulence, and energy partitioning, as provided in Table 1. The values for c_1 , c_2 , σ_1 , and σ_2 are taken from Hoppock et al. (2018).

The AWSoM model is split into two components: a solar corona (SC) and an inner heliosphere (IH) that are coupled via the Space Weather Modeling Framework (Tóth et al. 2012). For the SC component, we use a spherical grid ranging from $1 R_{\odot}$ to $24 R_{\odot}$. The grid is highly refined in the radial direction toward the Sun to numerically resolve the steep density gradients in the transition region. The smallest radial grid spacing is approximately $0.001 R_{\odot}$. In addition, we artificially broaden the transition region, similar to Lionello et al. (2009) and Sokolov et al. (2013). The domain is decomposed with adaptive mesh refinement (AMR) using grid blocks with $6 \times 8 \times 8$ internal grid cells for the radial, longitude, and

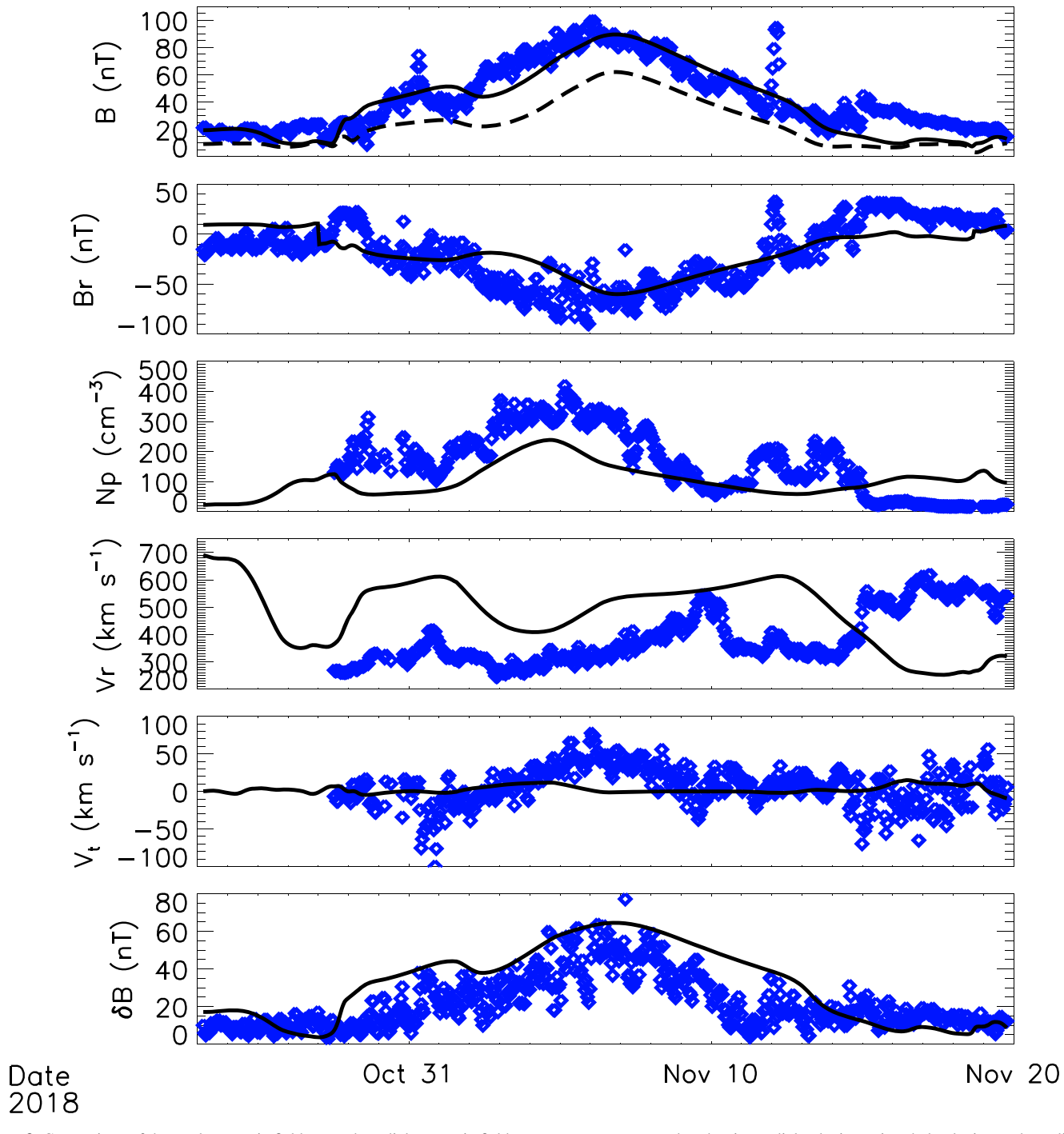


Figure 3. Comparison of the total magnetic field strength, radial magnetic field component, proton number density, radial velocity, azimuthal velocity, and amplitude of Alfvén wave magnetic field perturbation of the AWSoM output (black drawn lines) with the hourly PSP data (blue diamonds). The AWSoM background field strength without Alfvén magnetic field fluctuations is indicated by a dashed line.

latitude directions. At the base level, we have $16 \times 16 \times 8$ AMR blocks. For $r < 1.7\,R_\odot$, we refine the grid with one extra AMR level, so that the angular resolution is 1°.4 for both the latitude and longitude near the Sun, and 2°.8 outside. For the heliospheric current sheet (HCS), we apply four levels of refinement on top of the base level grid, resulting in angular grid spacing around the HCS of 0°.18 for both the latitude and longitude. The total number of cells in the SC component is 29.7 million. The IH domain is a square box, which extends from $-250\,R_\odot$ to $250\,R_\odot$ in the $X,\,Y,\,$ and Z directions. The

domain is decomposed using grid blocks with $8\times8\times8$ internal cells. The AMR is set up in such a way that we refine most near the coupling with SC and near the HCS. The cell size varies from $0.06\,R_\odot$ to $7.8\,R_\odot$. The total number of cells in the IH component is 33.8 million.

We iterate the SC and IH of AWSoM to converge to steady state in the Heliographic rotating (HGR) coordinate system. In Figure 2, the resulting HCS is colored with the radial solar wind speed. The magenta line is the PSP trajectory in the frame corotating with the Sun during the encounter time ranging from

2018 October 31 through November 12. According to the simulations, PSP crossed the HCS approximately at 2018 October 28 UT 00:30 and 2018 November 18 UT 16:00. Between these two times, PSP was to the south of the HCS. In the PSP observational data, multiple HCS crossings are listed in Szabo et al. (2020). From 2018 October 24 to November 20, the start times of HCS crossings for the inbound are 2018 October 28 03:01:19, 2018 October 29 10:49:42, and 2018 October 29 13:01:30. The crossings for the outbound are 2018 November 13 07:12:25, 2018 November 13 12:02:32, 2018 November 13 13:05:36, 2018 November 13 13:38:57, 2018 November 13 13:05:36, 2018 November 13 16:21:31, and 2018 November 14 11:12:53. The inbound crossing of the simulation corresponds well with the observations. The outbound crossing is off by about 5 days.

In Figure 3, we compare the field strength, the radial component of the magnetic field (Bale et al. 2016), proton number density, radial solar wind speed, azimuthal velocity, and magnetic field fluctuations of the Alfvén waves between the AWSoM output (in black lines) and the data of PSP, averaged in 1 hr periods (blue diamonds). Here, we use the proton moment data observed by the Solar Probe Cup, which is one instrument of the SWEAP instrument suite (Kasper et al. 2016). The plasma data cadence is as follows: high cadence is 0.874 s during Encounter mode, and low cadence is 27.962 s during Cruise mode (Kasper et al. 2019; Case et al., 2020). We use the magnetic field data from FIELDS, and the magnetic field data cadence is down-sampled to plasma cadence, and their initial time resolution varies between 2.3 Hz and 293 Hz (Bale et al. 2019). All data quality flags are used to filter the best measurements. The magnetic field fluctuations of the PSP data were obtained by taking the standard deviation for 1 hr data of each of the three magnetic field components and then calculating the magnitude using the field fluctuation components. Hence, the longitudinal component is included. The magnetic field fluctuations of the AWSoM output were calculated under the assumption that the reflected Alfvén wave energy density is small compared to the energy density of the outward-propagating Alfvén wave, so that the kinetic and magnetic energy of the fluctuations are the same. For the field strength, we show for AWSoM the total field strength $\sqrt{B^2 + \delta B^2}$ (drawn black line) and unperturbed magnetic field strength B (dashed line). The total field strength agrees very well with the PSP data. The AWSoM proton number density peak value of 239 cm⁻³ is lower than the PSP data by almost 100 cm⁻³, but the location of the peak is correct. The radial speed is overall a bit too high compared to the PSP data. The higher resolution near the heliospheric current sheet did lower the density and increase the speed at the PSP perihelion compared to van der Holst et al. (2019). The density and radial speed at the PSP perihelion could be improved by changing the Alfvén wave poynting flux at the inner boundary. However, in the present study we did not optimize for the poynting flux, but instead used the same default value of $(S_A/B)_{\odot} = 10^6$ $Wm^{-2}T^{-1}$ as in van der Holst et al. (2019). We also do not recover the surprising finding from the PSP observations that the azimuthal velocity is large near the PSP perihelion, with peaks at 35 km/s to 50 km/s. AWSoM shows rotational velocities of a few km/s. The Alfvén wave magnetic fluctuations of AWSoM agree very well with the fluctuations in the data, suggesting that AWSoM captures the solar wind turbulence well.

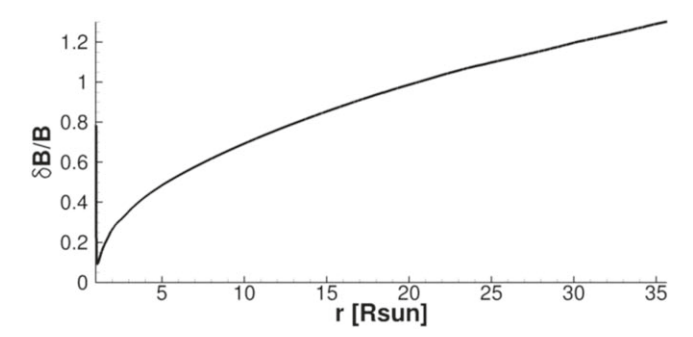


Figure 4. The ratio of $\delta B/B$ along the field line that traces the PSP perihelion location back to the Sun. Here, the field line is parameterized with the radius.

Figure 3 shows that $\delta B \sim B$ at perihelion both in the model output and the PSP data, hence the linear theory for energy partitioning used in the model may potentially be inaccurate. However, the $\delta B/B$ ratio is smaller near the Sun. In Figure 4, we plot this ratio along the field line that connects the PSP perihelion with the Sun. Very close to the Sun, where the coronal temperatures quickly increase to 1 MK and above, this ratio is smaller. Hence, the used energy partitioning is appropriate to obtain the coronal temperatures, but not necessarily the further evolution in the inner heliosphere.

In Figure 5, we compare isotropized, parallel, and perpendicular proton temperatures, proton temperature anisotropy, and parallel proton plasma beta between AWSoM (drawn lines) and hourly PSP data (blue diamonds). The temperature components and anisotropy data are fitted with the proton moment temperatures as a function of the magnetic field variations in the radial direction, with the method described in Huang et al. (2020). The fitted temperature anisotropy data have two cadences: the 10 s data set is generated with high-cadence plasma and magnetic field data, and the 1 minute data set is generated with low-cadence data, and the best fits are selected with the selection criteria described in Huang et al. (2020). The temperature anisotropy ratio of AWSoM is somewhat lower than the PSP data throughout most of the time range. This is an improvement compared to the simulations performed in van der Holst et al. (2019). There, the proton temperature anisotropy was significantly lower and stayed below 0.6 along the entire simulated PSP trajectory. In van der Holst et al. (2019), the parallel plasma beta $(\beta_{\parallel p})$ was predicted to be above 5 along the entire trajectory. In our new improved AWSoM, $\beta_{\parallel p}$ is much smaller, reaching values as low as 0.24, which is much closer to the observed $\beta_{\parallel p}$.

While the plasma was predicted to be firehose unstable along the entire PSP trajectory in van der Holst et al. (2019), this is no longer the case with the improved AWSoM simulations. In Figure 6, we show the observed distribution of $(\beta_{\parallel p}, T_{\perp p}/T_{\parallel p})$ values in color using the original high-cadence PSP data, and with black diamonds we show the simulated PSP trajectory in the $(\beta_{\parallel p}, T_{\perp p}/T_{\parallel p})$ -plane. From this comparison, we infer that $\beta_{\parallel p}$ is overall a bit too high and $T_{\perp p}/T_{\parallel p}$ is a bit too low. We also plot the mirror (Tajiri 1967), ion-cyclotron (Kennel & Petschek 1966), and parallel and oblique firehose marginal stability curves, for which the threshold values are taken from Verscharen et al. (2016). We note that we ran AWSoM with the less restrictive CGL firehose instability (Chew et al. 1956) instead of the parallel and oblique firehose instabilities. Part of the trajectory is now in the stable plasma region, and the plasma shows anticorrelation between $T_{\perp p}/T_{\parallel p}$ and $\beta_{\parallel p}$. Anticorrelation

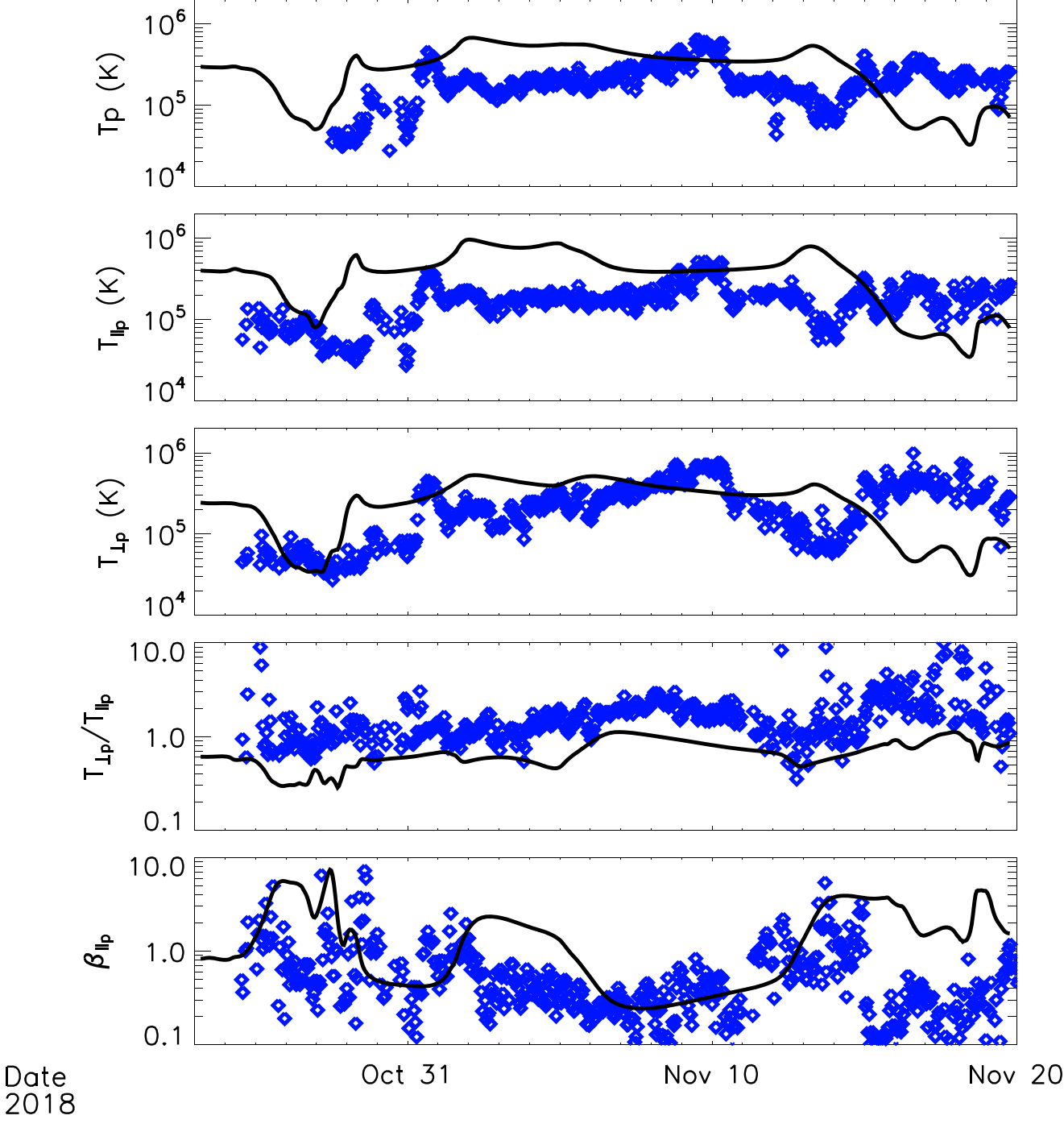


Figure 5. Comparison of the isotropized, parallel, and perpendicular proton temperature, proton temperature anisotropy, and parallel proton plasma beta $(\beta_{\parallel p})$ of the AWSoM output (black drawn lines) with the hourly PSP data (blue diamonds).

was shown for the fast wind by Marsch et al. (2004) and Hellinger & Trávníček (2014). We note that the simulated radial bulk speed at the PSP location was during the entire encounter in the superAlfvénic regime: $u_r/V_A \ge 3.3$.

To infer from what sources on the solar surface the solar wind observed by PSP originated, we perform field line tracing from the PSP locations back to the Sun. We selected 13 days around perihelion, 2018 November 6 UT 03:27, and use the PSP locations as the starting points to determine field line connectivity. In Figure 7, we show the top view of the mapping from the PSP to the solar surface, and limit it to a subset of six

field lines for clarity. The PSP trajectory is shown in magenta. The resulting field lines are all directed inward. In Figure 8, we show the zoom-in of the equatorial view. The field lines all connect to a negative-polarity region about the equator. The longitude and latitude at the solar surface can be found in Table 2.

5. Summary

We present a revised simulation of the first PSP encounter with our improved AWSoM model in combination with

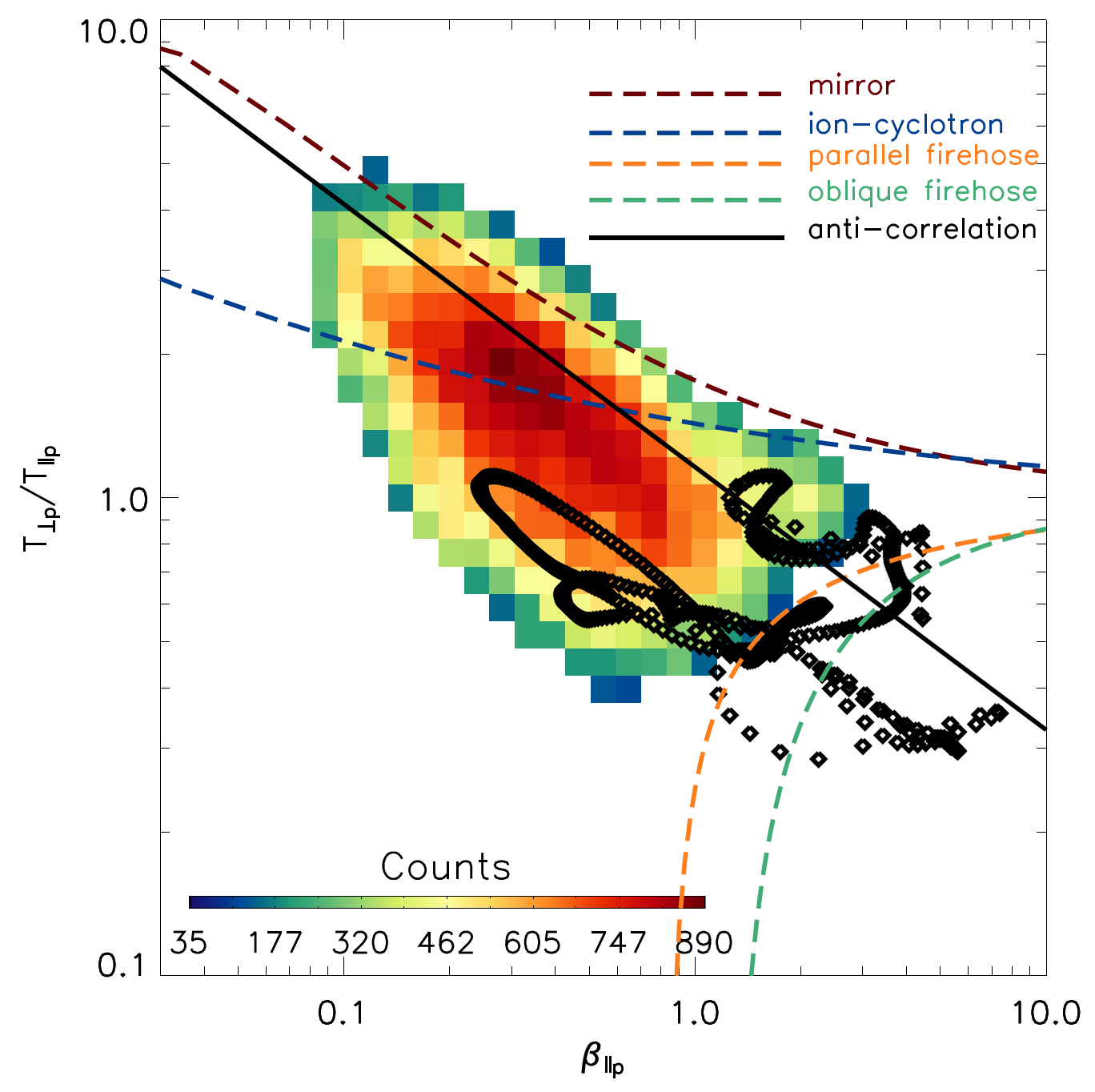


Figure 6. Observed distribution of $(\beta_{\parallel p}, T_{\perp p}/T_{\parallel p})$ values in color, and in black diamonds the simulated PSP trajectory in the $(\beta_{\parallel p}, T_{\perp p}/T_{\parallel p})$ -plane.

ADAPT–GONG maps. The first change made was significantly increasing the numerical resolution near the HCS to minimize the impact of discretization errors. Previously, the lower resolution resulted in a sizeable distorted region of the HCS characterized by disconnected V-shaped field lines, reduced magnetic field strength, and depleted Alfvén wave turbulence. The new grid has a resolution that is eight times finer near the HCS than our previous PSP simulations in van der Holst et al. (2019). The second major improvement was to revise the energy partitioning to increase both electron and parallel proton heating, which improves the solar corona and inner heliosphere solution outside of the finite-width HCS.

We have compared the improved AWSoM simulations with the PSP data. The quantities that match best are the total magnetic field strength, Alfvén wave fluctuations, and parallel plasma beta. The simulated proton temperature anisotropy ratio has increased compared to our PSP predictions (van der Holst et al. 2019), but is still lower than observed. Another major difference with our previous simulations is that due to the much smaller parallel plasma beta (order 1 instead of order 10), the simulated PSP plasma is no longer entirely firehose unstable.

We have also performed field line tracing from the spacecraft back to the solar surface to determine the source of the solar wind plasma observed by PSP. We find that around perihelion, the simulated field lines at PSP connect back to a negativepolarity region about the equator.

The improved energy partitioning was validated in Sachdeva et al. (2019) with EUV and SOHO/LASCO data and with IPS observations and OMNI data near Earth. The improvement also brought the polar-directed fast wind speed down to observed

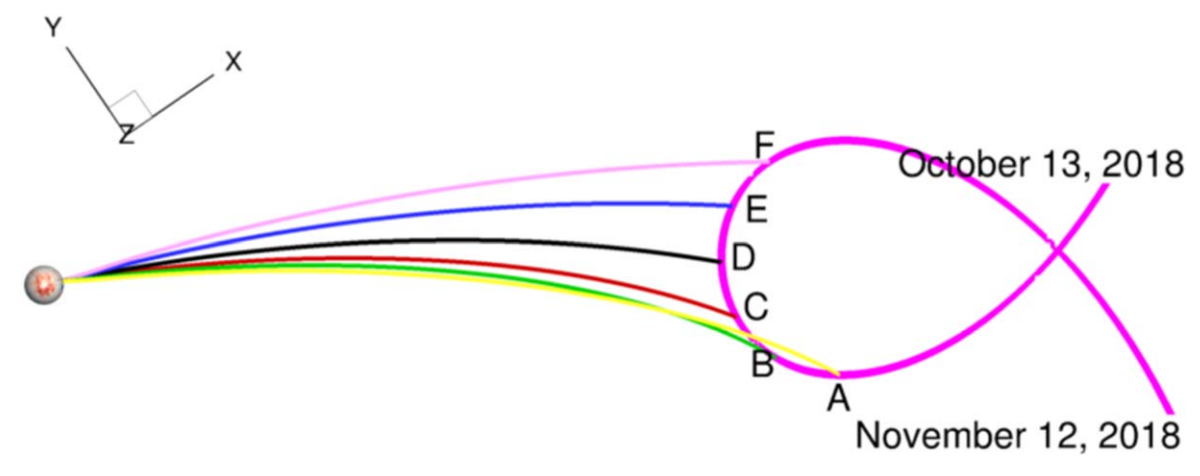


Figure 7. Top view of the field line mapping from the PSP's location back to the solar surface. The universal time associated with field lines A through F can be found in Table 2. All shown field lines are directed inward.

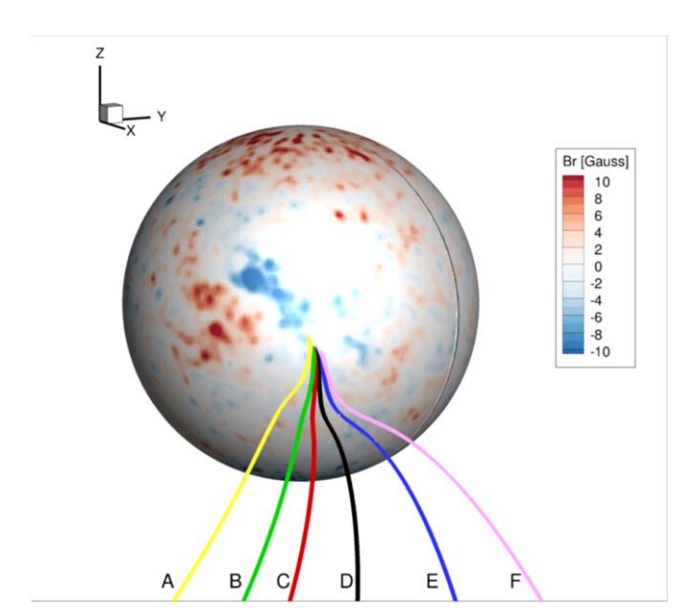


Figure 8. Zoom-in of the equatorial view of the field line mapping from the PSP's location back to the solar surface. The field lines A through F are the same as in Figure 7.

Table 2
Carrington Longitudes and Latitudes at the Solar Surface of the Field Lines A through F Shown in Figures 7 and 8

Field Line	Time	Longitude	Latitude
	2018 October 31 UT 03:27	335.3	2.6
	2018 November 1 UT 03:27	334.4	3.3
	2018 November 2 UT 03:27	334.3	2.3
A	2018 November 3 UT 03:27	335.5	-1.5
В	2018 November 4 UT 03:27	336.3	-4.1
C	2018 November 5 UT 03:27	336.7	-5.3
D	2018 November 6 UT 03:27	337.0	-5.5
E	2018 November 7 UT 03:27	337.6	-5.9
F	2018 November 8 UT 03:27	337.9	-5.4
2018 November 9 UT 03:27 2018 November 10 UT 03:27 2018 November 11 UT 03:27 2018 November 12 UT 03:27	337.9	-4.3	
	2018 November 10 UT 03:27	337.2	-2.6
	2018 November 11 UT 03:27	336.3	-0.05
	2018 November 12 UT 03:27	334.6	3.2

Note. The tabulated time is the universal time at which the PSP location is mapped back to the solar surface.

Ulysses levels from the $1000+km s^{-1}$ speeds shown in Jian et al. (2016).

We note that the model presented here used the first realization of the ADAPT-GONG magnetogram. While this map was the best choice in our PSP prediction paper (van der Holst et al. 2019), with the model improvements and better grid resolution this might no longer be the case. In future work, we will need to readdress the selection of the ADAPT realization. Additionally, the AWSoM model currently only incorporates the CGL version of the firehose instability. The more stringent parallel and oblique firehose instabilities would result in less anisotropy in the proton temperatures. We will address this limitation in a forthcoming paper.

This work was supported by the NSF grant 1663800 and PHY-2027555 and NASA grants NNX17AI18G, NNX16-AL12G, 80NSSC20K0600, 80NSSC20K0185, and 80NSSC17K0686. The simulations were performed on the NASA Advanced Supercomputing system Pleiades and the NSF sponsored TACC Frontera supercomputer. This work utilizes data produced by the NASA PSP from both the Solar Wind Electrons Alphas and Protons (SWEAP) and Fields Experiment (FIELDS) instruments. We acknowledge the NASA Parker Solar Probe Mission and the SWEAP team led by J. Kasper for use of data. The FIELDS experiment on the Parker Solar Probe spacecraft was designed and developed under NASA contract NNN06AA01C. The FIELDS team acknowledges the contributions of the Parker Solar Probe mission operations and spacecraft engineering teams at the Johns Hopkins University Applied Physics Laboratory. PSP/ FIELDS data is publicly available at http://fields.ssl.berkeley. edu/data/. We use synchronic magnetograms produced collaboratively between AFRL/ADAPT and NSO/NISP.

ORCID iDs

B. van der Holst https://orcid.org/0000-0001-5260-3944 J. Huang https://orcid.org/0000-0002-9954-4707 N. Sachdeva https://orcid.org/0000-0001-9114-6133 J. C. Kasper https://orcid.org/0000-0002-7077-930X

W. B. Manchester IV https://orcid.org/0000-0003-0472-9408

D. Borovikov https://orcid.org/0000-0002-0151-7437

B. D. G. Chandran https://orcid.org/0000-0003-4177-3328

A. W. Case https://orcid.org/0000-0002-3520-4041
K. E. Korreck https://orcid.org/0000-0001-6095-2490
D. Larson https://orcid.org/0000-0001-5030-6030
R. Livi https://orcid.org/0000-0002-0396-0547
M. Stevens https://orcid.org/0000-0002-7728-0085
P. Whittlesey https://orcid.org/0000-0002-7287-5098
S. D. Bale https://orcid.org/0000-0002-1989-3596
M. Pulupa https://orcid.org/0000-0002-1573-7457
D. M. Malaspina https://orcid.org/0000-0003-1191-1558
J. W. Bonnell https://orcid.org/0000-0002-0675-7907
K. Goetz https://orcid.org/0000-0003-0420-3633
R. J. MacDowall https://orcid.org/0000-0003-3112-4201

References

```
Al-Haddad, N., Lugaz, N., Poedts, S., et al. 2019, ApJ, 884, 179
Badman, S. t., Bale, S. D., Martínez Oliveros, J. C., et al. 2020, ApJS, 246, 23
Bale, S. D., Badman, S. T., Bonnell, J. W., et al. 2019, Natur, 576, 237
Bale, S. D., Goetz, K., Harvey, P. R., et al. 2016, SSRv, 204, 49
Boldyrev, S. 2005, ApJL, 626, L27
Bowen, T. A., Mallet, A., Bale, S. D., et al. 2020, PhRvL, 125, 025102
Chandran, B. D. G., Dennis, T. J., Quataert, E., & Bale, S. D. 2011, ApJ,
   743, 197
Chandran, B. D. G., & Hollweg, J. V. 2009, ApJ, 707, 1659
Chandran, B. D. G., Quataert, E., Howes, G. G., Xia, Q., &
   Pongkitiwanichakul, P. 2009, ApJ, 707, 1668
Chen, C. H. K., Bale, S. D., Bonnell, J. W., et al. 2020, ApJS, 246, 53
Chew, G. F., Goldberger, M. L., & Low, F. E. 1956, in RSPSA, 236, 112
Chhiber, R., Usmanov, A. V., Matthaeus, W. H., & Goldstein, M. L. 2019a,
    pJS, 241, 11
Chhiber, R., Usmanov, A. V., Matthaeus, W. H., Parashar, T. N., &
   Goldstein, M. L. 2019b, ApJS, 242, 12
De Pontieu, B., McIntosh, S. W., Carlsson, M., et al. 2007, Sci, 318, 1574
Dmitruk, P., Matthaeus, W. H., Milano, L. J., et al. 2002, ApJ, 575, 571 Fox, N. J., Velli, M. C., & Balse, S. D. 2016, SSRv, 204, 7
Gary, S. P., Bandyopadhyay, R., Qudsi, R. A., et al. 2020, ApJ, 901, 160
Goldreich, P., & Sridhar, S. 1995, ApJ, 438, 763
Hellinger, P., & Trávníček, P. M. 2014, ApJL, 784, L15
```

```
Henney, C. J., Toussaint, W. A., White, S. M., & Arge, C. N. 2012, SpWea,
  10, S02011
Hickmann, K. S., Godinez, H. C., Henney, C. J., & Arge, C. N. 2015, SoPh,
  290, 1105
Hollweg, J. V. 1978, RvGSP, 16, 689
Hollweg, J. V. 1986, JGR, 91, 4111
Hoppock, I. W., Chandran, B. D. G., Klein, K. G., Mallet, A., &
   Verscharen, D. 2018, JPIPh, 84, 905840615
Huang, J., Kasper, J. C., Vech, D., et al. 2020, ApJS, 246, 70
Jian, L. K., MacNeice, P. J., Mays, M. L., et al. 2016, SpWea, 14, 592
Kasper, J. C., Abiad, R., Austin, G., et al. 2016, SSRv, 204, 131
Kasper, J. C., Bale, S. D., Belcher, J. W., et al. 2019, Natur, 576, 228
Kennel, C. F., & Petschek, H. E. 1966, JGR, 71, 1
Liewer, P., Vourlidas, A., Thernisien, A., et al. 2019, SoPh, 294, 93
Lionello, R., Linker, J. A., & Mikić, Z. 2009, ApJ, 690, 902
Lithwick, Y., Goldreich, P., & Sridhar, S. 2007, ApJ, 655, 269
Marsch, E., Ao, X.-Z., & Tu, C.-Y. 2004, JGR, 109, A04102
Matthaeus, W. H., Zank, G. P., Oughton, S., Mullan, D. J., & Dmitruk, P.
  1999, ApJ, 523, L93
Riley, P., Downs, C., Linker, J. A., et al. 2019, ApJL, 874, L15
Riley, P., Lionello, R., Caplan, R. M., Downs, C., Linker, J. A.,
  Badman, S. T., & Stevens, M. L. 2021, A&A, 650, A19
Sachdeva, N., van der Holst, B., Manchester, W. B., et al. 2019, ApJ,
  887, 83
Sokolov, I. V., van der Holst, B., Oran, R., et al. 2013, ApJ, 764, 23
Spitzer, L., & Härm, R. 1953, PhRv, 89, 977
Szabo, A., Larson, D., Whittlesey, P., et al. 2020, ApJS, 246, 47
Szente, J., Landi, E., Manchester, W. B., et al. 2019, ApJS, 242, 1
Tajiri, M. 1967, JPSJ, 22, 1482
Tóth, G., van der Holst, B., Sokolov, I. V., et al. 2012, JCoPh, 231, 870
van der Holst, B., Manchester IV, W. B., Klein, K. G., & Kasper, J. C. 2019,
   ApJ, 872, L18
van der Holst, B., Sokolov, I. V., Meng, X., et al. 2014, ApJ, 782, 81
Vásquez, A. M., Frazin, R. A., Vourlidas, A., Manchester, W. B.,
   van der Holst, B., Howard, R. A., & Lamy, P. 2019, SoPh, 294, 81
Velli, M. 1993, A&A, 270, 304
Verscharen, D., Chandran, B. D. G., Klein, K. G., & Quataert, E. 2016, ApJ,
  831, 128
Vourlidas, A., Howard, R. A., Plunkett, S. P., et al. 2016, SSRv, 204, 83
Xiong, M., Davies, J. A., Feng, X., et al. 2018, ApJ, 868, 137
Zank, G. P., Matthaeus, W. H., & Smith, C. W. 1996, JGR, 101, 17093
```